

# The Global Conductivity Structure of the Lunar Upper and Midmantle

**Journal Article****Author(s):**

Mittelholz, Anna; Grayver, Alexander ; Khan, Amir; Kuvshinov, Alexey

**Publication date:**

2021

**Rights / license:**

[Creative Commons Attribution-NonCommercial 4.0 International](#)

**Originally published in:**

Journal of Geophysical Research: Planets 126(11), <https://doi.org/10.1029/2021JE006980>

**Key Points:**

- We study the time-varying magnetic field environment in lunar orbit using Lunar Prospector and Kaguya Selene magnetometer data
- We derive the first global radial electrical conductivity profile of the lunar upper and midmantle
- Estimated electrical conductivities in the lunar midmantle are similar to local Apollo-based models

**Correspondence to:**

A. Mittelholz,  
anna.mittelholz@erdw.ethz.ch

**Citation:**

Mittelholz, A., Grayver, A., Khan, A., & Kuvshinov, A. (2021). The global conductivity structure of the lunar upper and midmantle. *Journal of Geophysical Research: Planets*, 126, e2021JE006980. <https://doi.org/10.1029/2021JE006980>

Received 23 JUN 2021

Accepted 8 OCT 2021

**Author Contributions:**

**Methodology:** A. Grayver, A. Kuvshinov

**Writing – review & editing:** A. Grayver, A. Khan, A. Kuvshinov

## The Global Conductivity Structure of the Lunar Upper and Midmantle

A. Mittelholz<sup>1</sup> , A. Grayver<sup>1</sup> , A. Khan<sup>1,2</sup> , and A. Kuvshinov<sup>1</sup>

<sup>1</sup>Institute of Geophysics, ETH Zurich, Zurich, Switzerland, <sup>2</sup>University of Zurich, Physik-Institut, Zurich, Switzerland

**Abstract** Magnetic sounding is a powerful tool to explore the interior of planetary bodies through the electrical conductivity structure. The electrical conductivity structure of the lunar mantle has previously been derived from surface magnetic field measurements as part of the Apollo 12 mission and concurrent magnetometer data acquired from orbit through the Explorer 35 satellite. Here, we derive the first global conductivity structure of the upper and midmantle using only satellite magnetometer data collected by the recent Lunar Prospector and Kaguya Selene satellite missions. We show that the field in the geomagnetic tail exhibits a simple geometrical structure and can be well described by a single spherical harmonic of degree and order one. Employing this information about the inducing field geometry and assuming a potential representation of the field in the geomagnetic tail, we derive a frequency-dependent transfer function and invert it for a one-dimensional (1-D) electrical conductivity profile of the lunar upper and midmantle. Our global transfer function shows striking similarity with the local one obtained from joint analysis of Apollo 12 and Explorer 35 magnetometer data. This indicates the lack of local variations at the Apollo 12 landing site compared to the globally averaged upper to midmantle electrical conductivity structure.

**Plain Language Summary** Exploring the interior structure of planetary bodies is exceptionally difficult. However, traditionally geophysical methods have allowed us to gain insight by using various techniques, including magnetic sounding. In this study, we use satellite magnetic field data to constrain the electrical conductivity structure of the Moon. Electrical conductivity is an intrinsic material property that is sensitive to temperature, composition, and volatile content. Magnetic sounding relies on the fact that time-varying external magnetic fields induce electric currents and thus secondary magnetic fields in the subsurface, both of which can be measured by a lander or satellite. While it is challenging to separate the inducing field from the induced response, we find that when the Moon is in the geomagnetic tail, the organized nature of the inducing field allows us to get a magnetic transfer function and invert it for global conductivity with depth. Our model suggests that the lunar upper mantle at the Apollo landing site is representative of the average global structure.

### 1. Introduction

Electromagnetic induction sounding of planetary bodies allows us to infer their electrical conductivity structure that, in turn, enables constraints to be placed on parameters that bear directly on lunar formation and evolution such as temperature and composition (Khan et al., 2006; Verhoeven et al., 2005; Xu et al., 2000).

Since 1959 several missions have successfully measured lunar magnetic fields at the surface, in orbit, or in passing the Moon. Most notably during the Apollo missions magnetic field data were collected from the surface at three landing sites (12, 15, and 16), while satellites provided concurrent measurements from orbit (Sonett, 1982). More recently, Lunar Prospector (LP; Hood et al., 2001) and Kaguya Selene (KS; Takahashi et al., 2009) orbiters have mapped the magnetic field around the Moon from low-altitude orbits providing global coverage.

The observation of induced magnetic fields in the Moon, that is, secondary magnetic fields that are produced by currents flowing within the Moon as a result of variations in the external magnetic field, have formed the basis for studies seeking to constrain mantle electrical conductivity structure and the size of a highly conducting metallic core. The general principle behind magnetic sounding revolves around the concept of the transfer function as a means of obtaining information on subsurface electrical conductivity

© 2021 The Authors.

This is an open access article under the terms of the [Creative Commons Attribution-NonCommercial License](#), which permits use, distribution and reproduction in any medium, provided the original work is properly cited and is not used for commercial purposes.

structure. The transfer function incorporates information on the ratio of induced (internal) to inducing (external) fields, in addition to the geometry of the inducing field. Early studies relied on magnetometer data collected during the Apollo missions in combination with those collected from orbit (Dyal et al., 1974, 1976; Hobbs et al., 1983; Hood et al., 1982a; Sonett, 1982; Sonett et al., 1971).

Concurrent measurements of orbital data from Explorer 35 and Apollo 12 surface magnetic field measurements, covering the frequency range between  $5 \times 10^{-4}$  and  $4 \times 10^{-2}$  Hz (equivalent to periods between 25 and 2,000 s) (Hobbs, 1973, 1977; Sonett et al., 1972), allowed sounding to midmantle depths. Improved analysis led to an extension to lower frequencies ( $10^{-3}$ – $10^{-5}$  Hz), enabling sounding of the deeper lunar mantle (Hobbs et al., 1983; Hood et al., 1982a). Note that although Apollo 15 and 16 were also equipped with magnetometers, only the Apollo 12 magnetometer data were used for estimating transfer functions because of rapid degradation of the Explorer 35 magnetometers with time after the Apollo 12 mission had ended (Daily & Dyal, 1979).

The electrical conductivity structure and the average crust were found to be electrically resistive, with conductivities around  $10^{-9}$  S/m at the Apollo 12 landing site (Dyal et al., 1976; Sonett et al., 1971), while mantle electrical conductivity ranges between  $10^{-4}$  and  $10^{-9}$  S/m for the upper mantle and  $10^{-2}$ – $10^{-4}$  S/m for the midmantle and lower mantle (Dyal et al., 1976; Grimm & Delory, 2012; Hood et al., 1982a, 1982b; Khan et al., 2006, 2014), equivalent to Earth's lithosphere (Guzavina et al., 2019).

A number of studies have also estimated the lunar core size from magnetic field data (Hood et al., 1999; Russell et al., 1981; Shimizu et al., 2013). They relied on the observation that when the Moon enters the relatively steady magnetic field in the geomagnetic tail from the highly perturbed solar wind and terrestrial magnetosheath, a sudden change in the magnetic field amplitude and direction occurred, inducing electrical currents in the Moon's interior. While the currents induced in the mantle decay within a few hours, the core-induced field decays much slower due to its higher conductivity (Sonett, 1982). These studies approximated the core as a perfect conductor overlain by an insulating mantle and were thereby able to provide an upper bound on the core radius of  $\sim 400$  km. Later seismic analysis confirmed these results and constrained the core size to  $330 \pm 20$  km (Weber et al., 2011).

Despite efforts to derive the local conductivity structure from surface and concurrent satellite data, and constrain the lunar core size, none of the aforementioned studies have attempted to derive the global conductivity structure of the lunar mantle from satellite data covering the entire Moon. Consequently, the focus of this study is on deriving a globally averaged conductivity profile representative of the lunar upper and midmantle constrained by satellite magnetic measurements from the two most recent satellite missions, Lunar Prospector and Kaguya Selene. An advantage of our magnetic sounding method, as will be shown, is that it does not require the magnetic field to be measured simultaneously, at both surface and satellite altitude, removing limitations that beset the earlier Apollo-based studies.

In the following, we detail the steps considered in deriving a new satellite-based lunar transfer function. In Section 2, we present the Lunar Prospector and Kaguya Selene satellite data sets and study the external magnetic field structure around the Moon to identify the dominant geometry of the inducing field. The theoretical tools for evaluating the transfer function, the resulting C-response and a comparison with an Apollo-based transfer function are described in Section 3. In Section 4, we invert the transfer function for electrical conductivity structure of the lunar mantle using two different approaches and compare our results with Apollo-based results. Note that it is not the purpose here to draw implications of our results for lunar thermal and compositional structure and its bearing on the origin of the Moon. For this, interested readers are referred to reviews by Hood and Zuber (2000), Jaumann et al. (2012), and Khan et al. (2013, 2014).

## 2. Available Data and the Lunar Plasma Environment

### 2.1. Satellite Data

Both, Lunar Prospector (LP; Hood et al., 2001) and Kaguya Selene (KS; Takahashi et al., 2009), carried a magnetometer in low-altitude orbit around the Moon providing global coverage. The orbital parameters and duration of both missions are summarized in Table 1. Both missions were in nearly circular orbits and spent their primary mission phase at an altitude of around 100 km. The periapsis was lowered during the

**Table 1**  
*Orbital Parameters for the Lunar Prospector (LP) and Kaguya Selene (KS) Satellites*

	LP	KS
Mission timeline	January 1998–July 1999	December 2007–June 2009
Nominal mission altitude	~100 km	~100 km
Extended mission altitude	12–48 km	8–63 km, mostly >35 km
Orbital period	~2 h	~2 h
Sampling rate	5 s (~0.27°)	4 s (~0.2°)

extended mission (Figures 1a and 1b). The amplitude of the measured field is generally higher for LP (Figures 1c and 1d). This is due to different solar activity levels during the missions as is evident from the F10.7 solar radio flux (Tapping, 2013). For the time frame of the LP mission, the F10.7 values showed increased amplitude and variability compared to the KS time span (cf. orange lines in Figures 1c and 1d).

## 2.2. Structure of the External Field

To derive the transfer function (Equations 7 and 8), we need to characterize the geometry of the external field, that is, justify the degree and order one geometry adopted in the next section (Equations 4–6).

On Earth, at periods longer than one day, the structure of the time-varying external field is mostly governed by the magnetospheric ring current and can be described (for an observer at the planet's surface or at an altitude of a low-orbit satellite) by a zonal spherical harmonic of degree one (Banks, 1969; Kuvshinov et al., 2021; Price, 1967; Olsen, 1999). This only involves coefficients  $q_1^0$  and  $g_1^0$  (cf. Equations 2 and 3). At

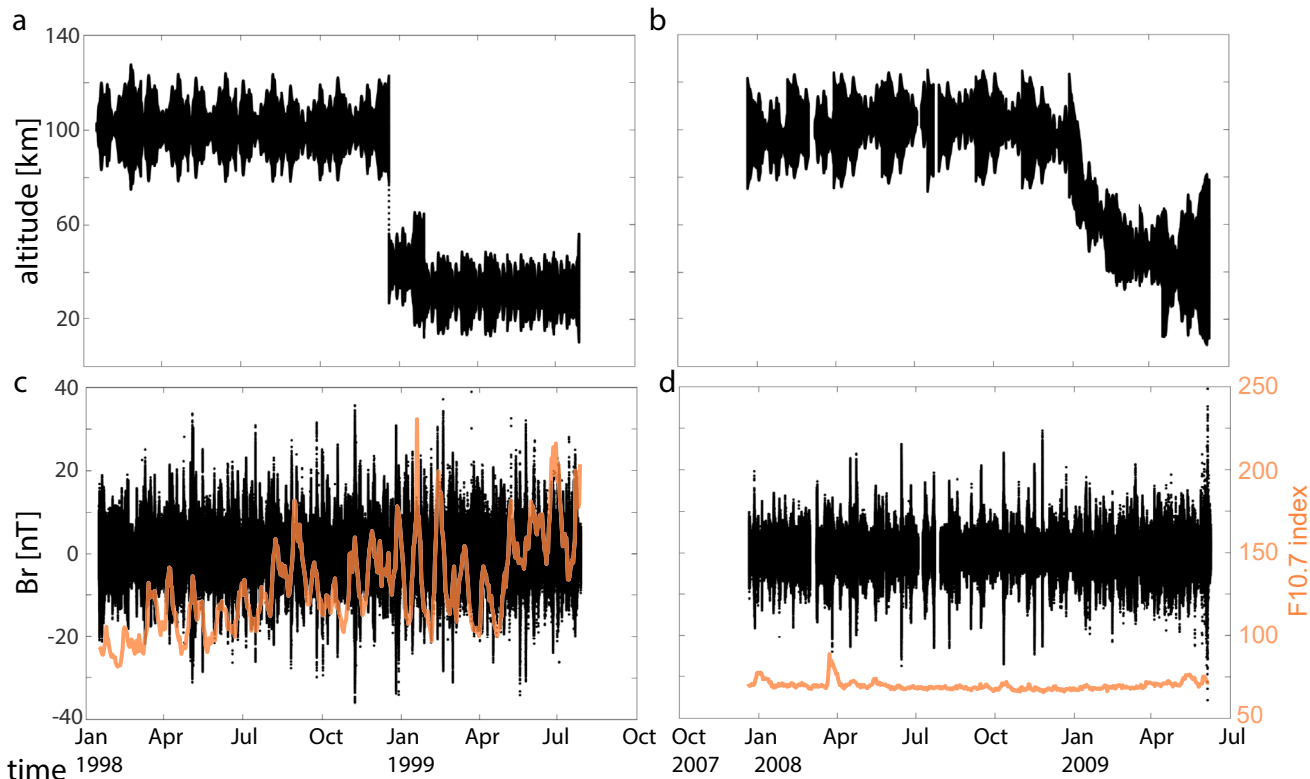


**Figure 1.** Altitude coverage of (a) Lunar Prospector and (b) Kaguya Selene missions and (c, d) respective radial magnetic field residuals (i.e., crustal field subtracted) in the Mean-Earth body-fixed frame. The right y-axis corresponds to the daily averaged values of the F10.7 index (orange), which describes solar radio flux at a wavelength of 10.7 cm.

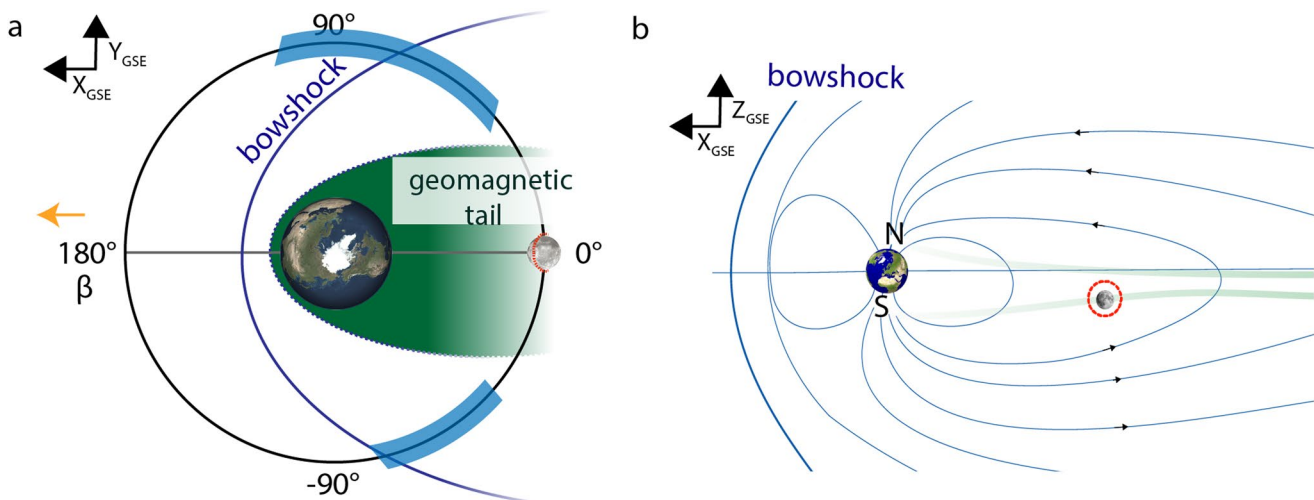


**Figure 2.** Schematic illustration of the Earth-Moon system with relevant orbital parameters. (a) Top view: The orbit angle,  $\beta$ , describes the Moon's position around the Earth and crosses the  $0^\circ$  point when the Moon is directly in the Sun-Earth line and thus in the geomagnetic tail. The orange arrow points toward the Sun. The red dashed line crossing the Moon shows a representative orbit of the selected missions. Blue shaded regions indicate the position of the Moon during swaths used for evaluation of Apollo dayside transfer functions (Hood et al., 1982a). The asymmetry is due to the westward position of Apollo 12 with respect to the Earth-Moon line. (b) Side view: The Moon in the geomagnetic tail with a representative satellite orbit (red dashed). The Geocentric Solar Ecliptic (GSE) coordinate system provides information on the Earth-Moon position with respect to the Sun. Not to scale.

periods between a few hours and one day, the time-varying external field is mostly due to currents flowing in the ionosphere.

In absence of an intrinsic lunar magnetosphere and ionosphere, the external field structure around the Moon is governed by different processes as illustrated in Figure 2. The Moon moves through two distinct regions. During more than half of the orbit, the Moon is in the solar wind plasma on the sun-facing part of the orbit and outside the bowshock (Figure 2a). Here, a potential representation of the magnetic field (cf. Equation 1) may not hold and the magnetic field does not exhibit a simple spatio-temporal structure. Within the bowshock, the Moon passes through the Earth's magnetosphere, including the magnetosheath and the magnetopause, and finally enters the geomagnetic tail (colored regions in Figures 2a and 2b). The time spent in the geomagnetic tail is  $\sim 3$  days (Ness et al., 1967); here, the potential representation is likely valid and, more importantly in the context of magnetic induction sounding, the inducing magnetic field exhibits a simple spatial structure, as will be shown below.

To examine the external field environment, we use the Geocentric Solar Ecliptic (GSE) coordinate system based on the Earth-Sun line. Here,  $X_{\text{GSE}}$  points from the Earth's center toward the Sun,  $Z_{\text{GSE}}$  is parallel to the upward normal of the Earth's ecliptic plane, and  $Y_{\text{GSE}}$  completes the right-handed system. Using the GSE frame, we further define the angle  $\beta$  as  $0^\circ$  when the Sun, the Earth, and the Moon are in one line and  $180^\circ$  when the Moon is between the Earth and the Sun (Figure 2a). This allows us to investigate how the magnetic field measured around the Moon changes as the Moon orbits the Earth during a lunation ( $\sim 28$  days; Figure 3).

To demonstrate that the Moon is exposed to a simple external magnetic field structure when it is in the geomagnetic tail field, we bin all residual data (i.e., after subtraction of the crustal magnetic field) in  $5^\circ$  orbital sectors for every lunation; this corresponds to 72 bins per lunation and about 9 hr of data per bin. Figure 3 shows the median of the magnetic field components for each bin. During a full orbit, the geomagnetic tail region is marked by a strong increase in  $B_{x,\text{GSE}}$ , which points toward or away from the Earth-Sun-line depending on which tail section the Moon is in. The components  $B_{y,\text{GSE}}$  and  $B_{z,\text{GSE}}$  are much smaller in this region. This effect is especially prominent in KS data (Figure 3b). The LP data set also exhibits this pattern, although the LP field is more disturbed outside of the tail region compared to KS measurements (Figure 3a). This is due to different solar activity levels during the missions (cf. orange lines in Figures 1c and 1d).

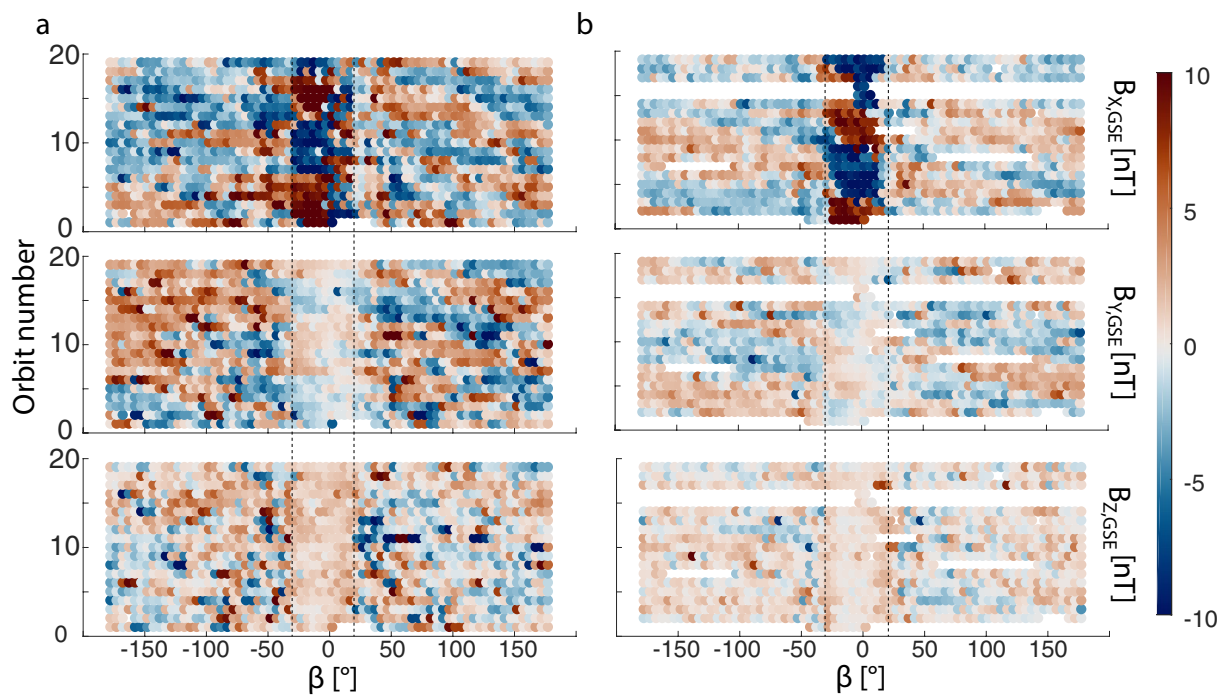


**Figure 3.** Binned components of the magnetic field in the Geocentric Solar Ecliptic frame for (a) Lunar Prospector and (b) Kaguya Selene. The orbit angle,  $\beta$ , describes a full lunar orbit around the Earth and crosses the zero point when the Moon is directly in the Sun-Earth line and thus in the geomagnetic tail. The dashed lines mark  $\beta$  at  $-30^\circ$  and  $20^\circ$ .

Each spacecraft crosses the tail region for every one of the respective 19 lunar orbits around the Earth. In the following, we will assume that the spacecraft is in the geomagnetic tail when the orbit angle  $\beta \in [-30^\circ, 20^\circ]$  (Figure 3). The asymmetry arises due to the tilt of the geomagnetic axis with respect to the Earth-Moon line and is noticeable in the data (Figure 3). The effect of seasons, that is, a tilt of the geomagnetic axis with respect to the ecliptic, leads to the Moon being in one tail lobe for consecutive orbits ( $\sim 6$  months; Figure 2), while the  $5^\circ$ -tilt of the lunar orbit around the Earth leads to the Moon being in one tail lobe (pointing in the  $-X_{\text{GSE}}$  direction) more often than in the other tail lobe (Figures 2b and 4a). The magnetic field in the geomagnetic tail ( $\beta \in [-30^\circ, 20^\circ]$ ) is dominated by  $B_{x,\text{GSE}}$  (Figures 4a and 4b) with minimal contributions in  $B_{y,\text{GSE}}$  and  $B_{z,\text{GSE}}$  (Figures 4a, 4c, and 4d); the bimodal distribution of  $B_{x,\text{GSE}}$  reflects the two different tail lobes, one pointing toward, one pointing away from the Sun. Low amplitudes  $B_{x,\text{GSE}}$  are also apparent when the satellite crosses the tail current sheet (Figure 4b). These observations are compatible with a source geometry dominated by the  $q_1^1$  and  $g_1^1$  Gauss coefficients (Equations 4–6). The selection of this subset of data results in 1,051 hr for the LP, and 1,005 hr for the KS missions.

### 3. Magnetic Transfer Functions

#### 3.1. Theoretical Background

Assuming that the observed magnetic field,  $\vec{B}$ , is a potential field,  $\vec{B}(\vec{r}, t) = -\nabla V(\vec{r}, t)$ , where  $V$  is a scalar potential. Thus, at a given location  $\vec{r} = (r, \theta, \phi)$  and time  $t$ , the field can be written as

$$\vec{B}(\vec{r}, t; \sigma) = -\nabla [V^e(\vec{r}, t) + V^i(\vec{r}, t; \sigma)], \quad (1)$$

where inducing and induced parts of the potential are given by

$$V^e(\vec{r}, t) = a \sum_{n=1}^{\infty} \sum_{m=0}^n [q_n^m(t) \cos(m\phi) + s_n^m(t) \sin(m\phi)] \left(\frac{r}{a}\right)^n P_n^m(\cos\theta) \quad (2)$$

and

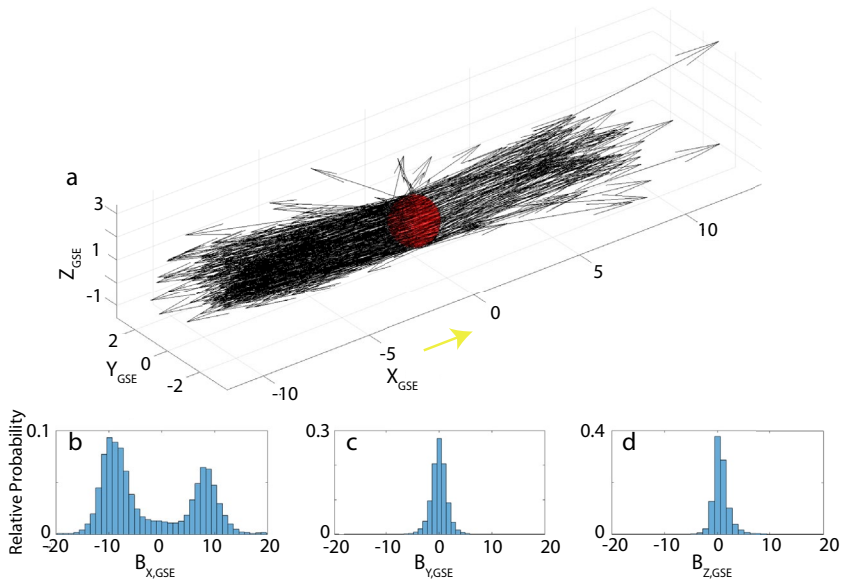


**Figure 4.** (a) Kaguya Selene geomagnetic tail data in the Geocentric Solar Ecliptic (GSE) frame with arrows depicting median magnetic field vectors binned in 0.2 lunar radii ( $\sim 350$  km)  $X_{\text{GSE}}$ ,  $Y_{\text{GSE}}$ , and  $Z_{\text{GSE}}$  bins. Arrows point in the  $+X_{\text{GSE}}$  or  $-X_{\text{GSE}}$  direction depending if the Moon is in the upstream or downstream geomagnetic tail and the yellow arrow points toward the Sun. (b–d) Histograms of magnetic field components.

$$V^i(\vec{r}, t; \sigma) = a \sum_{n=1}^{\infty} \sum_{m=0}^n [g_n^m(t; \sigma) \cos(m\phi) + h_n^m(t; \sigma) \sin(m\phi)] \left(\frac{a}{r}\right)^{n+1} P_n^m(\cos \theta), \quad (3)$$

respectively. Here  $q_n^m$ ,  $s_n^m$ , and  $g_n^m$ ,  $h_n^m$  describe external (inducing) and internal (induced) Gauss coefficients of degree  $n$  and order  $m$ ,  $a = 1737.1$  km is the mean lunar radius,  $P_n^m(\cos \theta)$  represents the Schmidt seminormalized associated Legendre functions, and  $r$ ,  $\theta$ , and  $\phi$  are coordinates of the spherical Mean-Earth (ME) reference system. This reference system is a body-fixed selenographic system for which the prime meridian (longitude  $\phi = 0^\circ$ ) is defined by the mean Moon-Earth direction (NASA, 2008).

For the particular case that the inducing magnetic field is uniform in space and parallel to the earthward pointing axis (i.e.,  $n = m = 1$ ), and further assuming that conductivity varies only radially, the magnetic field measured at a low-Moon-orbit can be approximated as

$$B_r(r, \theta, \phi, t) = - \left[ q_1^1(t) - 2g_1^1(t; \sigma) \left(\frac{a}{r}\right)^3 \right] \cos \phi \sin \theta, \quad (4)$$

$$B_\theta(r, \theta, \phi, t) = - \left[ q_1^1(t) + g_1^1(t; \sigma) \left(\frac{a}{r}\right)^3 \right] \cos \phi \cos \theta, \quad (5)$$

$$B_\phi(r, \theta, \phi, t) = \left[ q_1^1(t) + g_1^1(t; \sigma) \left(\frac{a}{r}\right)^3 \right] \sin \phi. \quad (6)$$

We can estimate the time series of inducing and induced coefficients  $q_1^1$  and  $g_1^1$  from Equations 4–6 by solving a minimization problem for a discrete set of time windows using robust least-squares.

Inducing and induced coefficients are linearly related in the frequency domain through a transfer function, the  $Q$ -response (Olsen, 1999). For inducing,  $q_1^1$ , and induced,  $g_1^1$ , this is

$$Q_1(\omega; \sigma) = \frac{\tilde{g}_1^1(\omega; \sigma)}{\tilde{q}_1^1(\omega)}, \quad (7)$$

where  $\tilde{q}_1^1$  and  $\tilde{g}_1^1$  are the frequency-domain counterparts of the time-domain coefficients. Note that the transfer function  $Q$  depends on the degree of the inducing field, frequency, and conductivity. From the  $Q_1$ -response, we can form a corresponding global  $C_1$ -response (in the text referred to as  $C$ -response) at the surface of the planet (Olsen, 1999)

$$C_1(a, \omega; \sigma) = \frac{a}{2} \frac{1 - 2Q_1(\omega; \sigma)}{1 + Q_1(\omega; \sigma)}. \quad (8)$$

Given time series of  $\tilde{q}_1^1$  and  $\tilde{g}_1^1$ , the transfer function (Equation 7) and uncertainties can be estimated by standard window-based sectioning followed by a robust least-squares spectral estimation. For more details on the spectral analysis we refer to Püthe and Kuvshinov (2014).

We note here that the potential field assumption stated in Equation 1 implies that satellites are in an insulating environment, such as vacuum. In reality, even in the geotail, lunar orbiters are in a low-density plasma (Baumjohann & Treumann, 1996). Hood and Schubert (1978) have studied the magnetohydrodynamic (MHD) effects for lunar settings with implications for induction sounding. The authors concluded that at sufficiently low frequencies ( $\omega \lesssim 10^{-3}$  Hz), the MHD effects are negligible and the field representation as in Equation 1 is justified.

### 3.2. Estimation of $C$ -Responses

We estimate  $C$ -responses by using the magnetic field measured in the geomagnetic tail. To ensure that the field of internal origin is the induced field, we need to minimize the contribution of all other internal magnetic field sources. Because the Moon presently has no core field, the only other internal source is the lunar crustal magnetic field and we subtract the model field of Ravat et al. (2020) from the data. This model is based on LP and KS along-track magnetic field gradients using equivalent source monopoles. We additionally excluded data around dusk and dawn because of vanishing sine and cosine terms in Equations 4–6. Specifically, we exclude longitudes around  $90^\circ \pm 20^\circ$  and  $270^\circ \pm 20^\circ$  and latitudes poleward of  $70^\circ$ .

From Equations 4–6, we can estimate the time series of inducing and induced coefficients  $q_1^1$  and  $g_1^1$  by solving the following minimization problem for a discrete set of time windows covering the LP and the KS time frame using robust least-squares

$$\min_{q_{1,j}^1, g_{1,j}^1} \sum_{t \in D_j} \sum_{\alpha \in \{r, \theta, \phi\}} \left| B_\alpha^{\text{obs}}(\vec{r}, t) - \{B_\alpha^{\text{ext}}(\vec{r}) + B_\alpha^{\text{int}}(\vec{r})\} \right|^2; \quad j = 1, 2, \dots \quad (9)$$

Here,  $B_\alpha^{\text{ext}}$  and  $B_\alpha^{\text{int}}$  correspond to the terms with  $q_1^1$  and  $g_1^1$ , respectively,  $N$  is the number of time windows, and  $\vec{r} \equiv \vec{r}(t)$ , since the satellites move in time. The notation  $t \in D_j$  indicates that we take all available measurements in a time window,  $D_j$ , of length  $\Delta t$

$$D_j \equiv [t_j - \Delta t/2; t_j + \Delta t/2], \quad t_j = (j - 1/2)\Delta t, \quad j = 1, 2, \dots, N.$$

We chose 2 hr for the length of a time window,  $\Delta t$ , which roughly corresponds to a single spacecraft orbit. This ensures wide latitudinal coverage whilst maximizing the length of the time series of the coefficients  $q_1^1$  and  $g_1^1$ . The time window also dictates the minimum resolvable period of the transfer function, whereas the maximum period is bounded by the time the spacecraft spent in the geomagnetic tail.

The estimated  $C$ -responses along with their associated uncertainties are shown in Figure 5a and tabulated in Table 2. The responses are obtained for periods between 7 and 44 hr. For a laterally homogeneous planet, the real part of the  $C$ -response is expected to monotonically increase with increasing period and the imaginary part should tend to zero for very long periods (Weidelt, 1972). Within the estimated uncertainties, our  $C$ -responses generally follow this behavior. The noticeably larger uncertainties at the two longest periods are most likely due to fewer time windows used for the estimation of  $C$ -responses. In line herewith, coherence is mostly around 0.5 except for the longest period where coherence drops significantly (Figure 5b).

The real part of the  $C$ -response serves as a proxy for the penetration depth of the electromagnetic field into the planetary body (Weidelt, 1972). At longer periods, the real part of the  $C$ -response will approach the depth of the core-mantle boundary asymptotically. The maximum observed period in this study thus

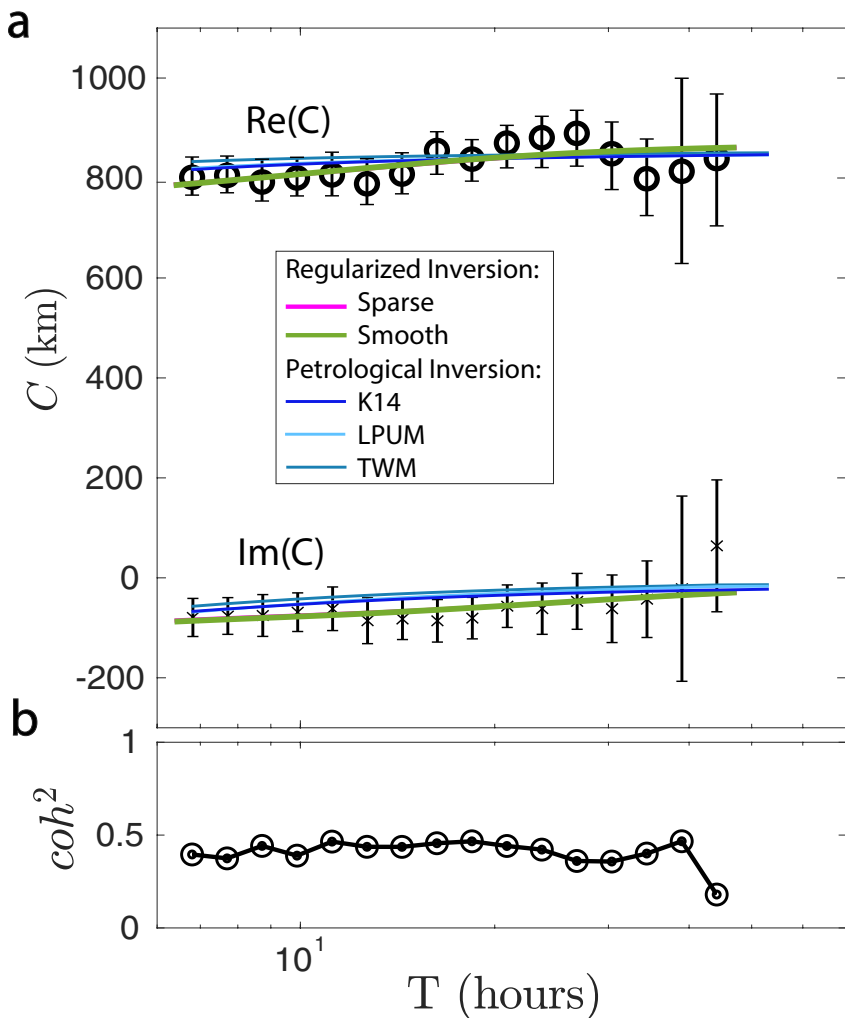


**Figure 5.** (a) Estimated real (circles) and imaginary (crosses) parts of  $C$ -responses with error bars, overlaid by modeled responses for the smooth (green) and sparse (pink) models of the regularized inversion and the blue models for the petrological inversion (Section 4). (b) Corresponding squared coherence.

limits us to investigating structure down to about 900-km depth. Our observed period range of 7–44 hr covers a range in which the associated  $C$ -response is relatively flat (consistent with Apollo results at overlapping periods shown in the next subsection). This is a consequence of the highly resistive lunar crust and upper mantle through which the electromagnetic field propagates with little attenuation. As a result, we are limited to sounding the electrical conductivity structure in the depth range of  $\approx$ 300–900 km. Note that from a methodological point of view, the  $C$ -response as stated in Equation 8 characterizes the subsurface conductivity globally. However, due to limitations imposed by the presently used satellite data, our model has the highest sensitivity in the 300–900-km depth range. Although no widely accepted classification of different regions of the lunar mantle is available, we attribute this depth range to the upper and mid-mantle.

### 3.3. Comparison With Apollo 12 Transfer Functions

A comparison between an Apollo-derived transfer function and ours is shown in Figure 6. Because the Apollo transfer function is only available in the form of apparent resistivity values (Hobbs et al., 1983; Hood et al., 1982a), we transform our complex-valued  $C$ -responses to an apparent resistivity curve using (Olsen, 1999).

**Table 2**

Real and Imaginary Parts of Estimated C-Responses ( $C_{\text{real}}$ ,  $C_{\text{imag}}$ ) With Uncertainties ( $dC$ )

Period (s)	$C_{\text{real}}$ (km)	$C_{\text{imag}}$ (km)	$dC$ (km)
24,469	803.9	-79.8	38.1
27,719	807.2	-76.9	36.7
31,402	795.8	-75.9	41.8
35,573	802.8	-69.3	38.6
40,298	808.0	-62.4	43.6
45,651	792.8	-86.4	45.8
51,715	809.4	-83.0	41.0
58,584	850.0	-86.5	42.6
66,366	835.3	-81.1	41.5
75,181	862.8	-57.3	42.5
85,168	872.1	-62.2	51.3
96,481	879.6	-47.6	55.9
109,297	844.5	-62.4	67.6
123,816	801.4	-43.3	76.6
140,262	814.3	-22.2	185.3
158,894	836.1	63.5	131.9

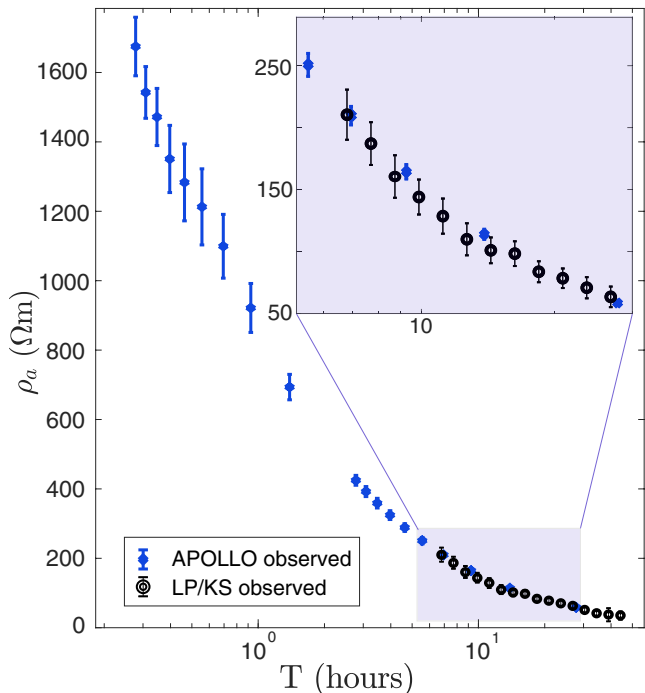


**Figure 6.** Apparent resistivity,  $\rho_a$ , from Apollo data (blue; Hobbs et al., 1983; Hood et al., 1982a) and from Kaguya Selene (KS)/Lunar Prospector (LP) of this study (black). The purple shaded region provides a zoom of the period range in which  $\rho_a$  estimates overlap.

$$\rho_a(\omega) = \omega\mu|C_1(\omega)|^2. \quad (10)$$

The comparison shows remarkable agreement between apparent resistivity values derived from our new satellite-based response and the local Apollo 12 transfer function across the overlapping frequency range.

In making this comparison, we have to be aware of a number of differences underlying the two approaches. Apollo transfer functions are based on data collected during the daytime, that is, when the Moon faces the Sun and is in a region where it is exposed to a highly conducting plasma (the blue shaded regions of the lunar orbit shown in Figure 2a). These parts of the lunar orbit exclude the region in the geomagnetic tail that is used in this study. Consequently, during the periods when the Moon is on the dayside, the observed magnetic field is not a potential field. Instead, Apollo-era studies (Hobbs et al., 1983; Hood et al., 1982a; Sonett, 1982) assume a spherical symmetric plasma (SSP) model and perfect confinement of the induced fields by the solar wind. This theory was developed to interpret the lunar dayside hemisphere where the induced field is confined within the lunar surface. It was recognized that the assumption of complete confinement is most likely not met in the wake region (Hobbs et al., 1983), which was considered problematic especially at high frequencies. With the SSP assumption, the external magnetic field is spatially uniform and can be described by spherical harmonic degree 1, while no assumption was made about the order. It was assumed that the Explorer 35 satellite measured the external inducing magnetic field from orbit ( $\bar{B}^e$ ), whereas the Apollo surface magnetometer measured both the external field and the induced field ( $\bar{B}^e + \bar{B}^i$ ) at the lunar surface. Because of the presence of the highly conducting plasma-layer between the satellite and the surface, the radial component is continuous, that is,  $B_r(r = a + h) = B_r(r = a)$ , where  $h$  and  $a$  are the height of the satellite orbit and the lunar radius, respectively. The transfer function can therefore be estimated from

$$T_\theta(\omega) = \left| \frac{B_\theta^e(\omega, a) + B_\theta^i(\omega, a)}{B_\theta^e(\omega, a + h)} \right| \quad (11)$$

and

$$T_\phi(\omega) = \left| \frac{B_\phi^e(\omega, a) + B_\phi^i(\omega, a)}{B_\phi^e(\omega, a + h)} \right|. \quad (12)$$

Finally,  $C$ -responses are obtained from  $|C| = a/2T_{\theta(\phi)}(\omega)$ , which can be converted to apparent resistivity through Equation 10.

In summary, our approach relies on the fact that the field can be approximated as a potential field for a subset of the data, which allows us to exploit the concept of global  $C$ -responses (Olsen, 1999). As a consequence, we estimate a complex-valued transfer function and thus retrieve both, apparent resistivity and phase from data collected by a single magnetometer. Although we use satellite data in this study, the approach can easily be adapted to estimate local  $C$ -responses from surface magnetic field data only (Munch et al., 2018).

**Table 3**  
*Bulk Lunar Composition Models*

Element	Khan et al. (2014)	Taylor (1982)	Longhi (2003)
CaO	4	4.6	3.18
FeO	11	10.9	7.62
MgO	35	32.7	38.3
Al <sub>2</sub> O <sub>3</sub>	4.5	6.14	3.93
SiO <sub>2</sub>	45	44.4	46.1
TiO <sub>2</sub>	0.5	0.31	0.17

*Note.* Compositional models are the Taylor Whole Mantle (Taylor, 1982), the Lunar Primitive Upper Mantle (Longhi, 2003), and the inverted bulk mantle composition corresponding to the highest posterior probability model from Khan et al. (2014). All quantities are given in wt. %.

## 4. Inverting for Electrical Conductivity Structure

We invert derived  $C$ -responses using two different approaches. The first approach is a conventional regularized inversion with no physics-based model constraints (Grayver & Kuvshinov, 2016), whereas the second is a mineral-physics constrained inversion after Khan et al. (2014). In the following, we refer to this second approach as petrological inversion.

### 4.1. Regularized Models

The radial conductivity profile is obtained by inverting the estimated global  $C$ -responses. We fix the electrical conductivity of the innermost 170 km to be  $10^5$  S/m and allow it to vary otherwise. The inversion is posed as a minimization problem

$$\min_{\mathbf{m}} [\phi_d(\mathbf{m}) + \gamma \phi_r(\mathbf{m})], \quad (13)$$

where  $\phi_d$  represents the standard least-squares data misfit,  $\phi_r$  is the regularization term scaled by a regularization parameter  $\gamma$ , and  $\mathbf{m} = (\ln \sigma_1, \ln \sigma_2, \dots, \ln \sigma_M)$  is the vector of unknown model parameters (the logarithm ensures that conductivity is positive).

The data misfit term is given by

$$\phi_d(\mathbf{m}) = \sum_{i=1}^N \frac{[d_{obs}^i - d_{cal}^i(\mathbf{m})]^2}{2\delta_i^2}, \quad (14)$$

where  $d_{cal}(\mathbf{m})$  and  $d_{obs}$  are the modeled and observed  $C$ -responses, respectively, both of which are evaluated at a discrete set of frequencies  $\omega_i$ ,  $i = 1, 2, \dots, N$ , and  $\delta$  is the uncertainty on observed  $C$ -responses. To model  $C$ -responses, the recursion formula from Kuvshinov and Semenov (2012) is used.

The regularization term is given by

$$\phi_r(\mathbf{m}) = \frac{1}{p_m} \sum_{i=1}^M |\mathbf{l}_i \mathbf{m}|^{p_m}, \quad (15)$$

where  $\mathbf{l}_i$  is a roughness operator of the  $i$ th model parameter and  $p_m$  is a model norm. In what follows, models derived with the model norm  $p_m = 1$  will be denoted “sparse” and models estimated with the norm  $p_m = 1.5$  are denoted “smooth.” The minimization problem is solved by using a global stochastic optimization method as discussed in detail in Grayver and Kuvshinov (2016).

### 4.2. Petrological Models

For the petrological models, we rely on the work of Khan et al. (2014), who explored lunar mantle compositions within the model chemical system CaO-FeO-MgO-Al<sub>2</sub>O<sub>3</sub>-SiO<sub>2</sub>-TiO<sub>2</sub> and computed geophysical properties from thermodynamic data for a given model pressure, temperature, and bulk composition by Gibbs energy minimization (Connolly, 2005). These calculations were made taking into consideration the stoichiometric solid phases and species in the thermodynamic data compilation of Holland and Powell (1998). Given the equilibrium mineralogy so computed, Khan et al. (2014) interfaced the latter with an electrical conductivity database to estimate radial bulk electrical conductivity profiles. In the inversions performed here, we make the assumption of fixed bulk composition. For this purpose, and in addition to the composition determined by Khan et al. (2014), we consider a set of established bulk lunar compositions based on the work of Taylor (1982) and Longhi (2003). The three compositions are listed in Table 3.

The inversion is conducted by using a stochastic method. Within a Bayesian framework, the solution to the inverse problem  $\mathbf{d} = g(\mathbf{m})$ , with data vector  $\mathbf{d}$  and operator  $g$  that maps model parameter  $\mathbf{m}$  into data, is described by (e.g., Mosegaard & Tarantola, 1995)

$$\eta(\mathbf{m}) = k h(\mathbf{m}) \mathcal{L}(\mathbf{m}), \quad (16)$$

where  $k$  is a normalization constant and  $h(\mathbf{m})$  is the prior probability distribution on model parameters containing information about model parameters independent of the data (cf. Section 6.4 in Khan et al. (2014)). The likelihood function,  $\mathcal{L}(\mathbf{m})$ , can be interpreted as a measure of how well the predictions fit the observations given a model  $\mathbf{m}$ , and, finally,  $\eta(\mathbf{m})$  represents the solution to the inverse problem. The likelihood function is given by

$$\mathcal{L}(\mathbf{m}) \propto \exp(-\phi_d(\mathbf{m})), \quad (17)$$

where  $\phi_d(\mathbf{m})$  is given by Equation 14. For detailed information on the inversion, we refer to Khan et al. (2014). In what follows, we limit ourselves to discussing the electrical conductivity structure, but would like to note that we have checked all output parameters for consistency with Khan et al. (2014).

## 5. Results and Discussion

The results from the inversion of the newly derived  $C$ -responses (hereafter referred to as LP/KS TFs) are shown in Figure 7. Within the period range  $\sim 7$ –44 hr, our global  $C$ -responses are sensitive to  $\sim 300$ –900 km in depth and based on global satellite data excluding dusk and dawn regions. The Apollo-based models of Hood et al. (1982a) and Khan et al. (2014) are shown for comparison. We show smooth and sparse models as members of the family of regularized solutions and both electrical conductivity models fall within the range of the Apollo-derived local conductivity profiles of Hood et al. (1982a), but are lower than those obtained by Khan et al. (2014). Both of the regularized models are very similar and show only minor differences below 700 km, where the sparse model predicts slightly lower conductivities, although the predicted  $C$ -responses (Figure 5a) are virtually indistinguishable. The regularized inversion model values are also listed in Table 4. The model obtained from the petrological inversion of the new responses (blue model in Figure 7a) is, like the regularized models, lower than the Apollo-based prediction of Khan et al. (2014). Consistent herewith, we find that petrological models based on the new LP/KS TFs and two other geochemically derived lunar compositions (Longhi, 2003; Taylor, 1982) also lead to lower conductivities in the upper and midmantle compared with the local Apollo-based models (light and dark blue models in Figure 7b). In contrast hereto, the conductivity profiles obtained from inversion of the Apollo TFs for the same two lunar compositions, are equivalent within uncertainties to the model of Khan et al. (2014) (cf. yellow and orange models in Figure 7b). As a first observation, this suggests differences in the Apollo and the LP/KS TFs, which, given the similarity of the apparent resistivity curves shown in Figure 5c, may appear counterintuitive.

Yet, there are important differences between our global and the Apollo 12 transfer functions. First, and as discussed in Section 3.3, Apollo TFs are only available in the form of apparent resistivity values with no phase information (Hobbs et al., 1983), whereas we inverted complex-valued  $C$ -responses. Second, Apollo TFs cover shorter periods (down to  $\sim 0.3$  hr; Figure 6) compared to our responses; consequently, the Apollo-based conductivity models are likely better constrained at shallower depths. Third, inferred conductivity model uncertainties are larger in the case of LP/KS TFs across most of the mantle, which is a consequence of the larger error bars of our global transfer function. Keeping this in mind, the observed differences between the Apollo-constrained and the LP/KS-constrained models should be interpreted with caution.

Our results indicate that the local electrical conductivity structure at the Apollo 12 landing site could be similar to or possibly slightly higher than the average electrical conductivity structure of the Moon at a depth range between  $\sim 300$  and 900 km, thus hinting at the absence of significant local variations in subsurface structure at least at this location. The Apollo 12 landing site is located in Oceanus Procellarum, which has been suggested to be a relict impact basin and the origin of the lunar dichotomy (Jutzi & Asphaug, 2011; Nakamura et al., 2012; Whitaker, 1981). This hypothesis would be suggestive of a locally different compositional and/or temperature profile in the region and associated differences in electrical conductivity values relative to a global estimate. We do not observe any evidence for this based on the current data. However,

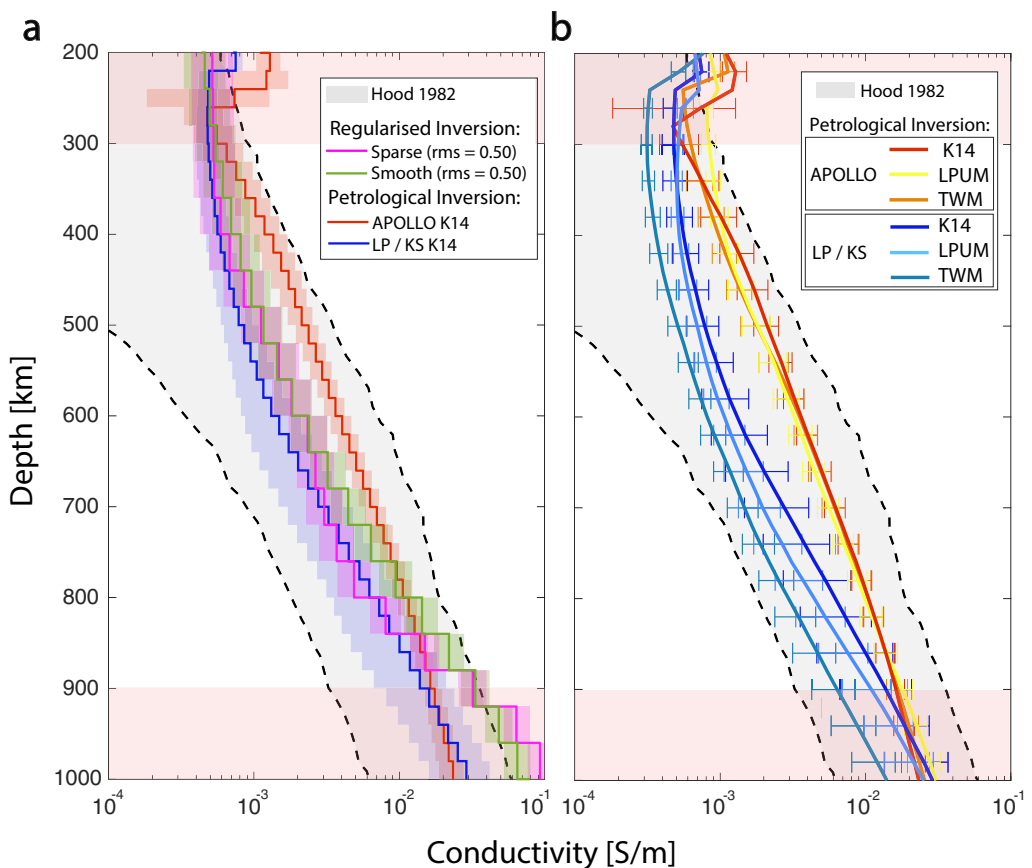


**Figure 7.** (a) Inverted smooth (green) and sparse (pink) models with upper and lower bounds (shaded). The gray shaded region (also in panel b) represents the conductivity range and bounds (black dashed) obtained from the former analysis of an Apollo transfer function (Hood et al., 1982a). For direct comparison, we also show results from the petrological models using the Khan14 composition, in combination with the Apollo (red) and LP/KS (blue) transfer functions. Note, that Apollo K14 corresponds to the previously published model by Khan et al. (2014). The area between 0–300 and 900–1,200 km is shaded (pink) to emphasize the lack of sensitivity at these depths. (b) Mean conductivity profiles with one standard deviation uncertainties using Apollo (red, orange, yellow), and LP/KS (blue tones) transfer functions with the Khan14 (K14), Taylor Whole Moon (TWM), and Lunar Primitive Upper Mantle (LPUM) compositional models. See legend.

because most of the remaining effects of the basin forming impact might affect shallower depths than 300 km, we cannot address the topic further with this study.

Understanding local variations in subsurface electrical conductivity structure is presently limited by the absence of magnetometer data for all Apollo missions. However, with recent efforts devoted to digitizing and archiving the data collected from all three Apollo magnetometers (12, 15, and 16) (Nagihara et al., 2020), the construction and comparison of local transfer functions stands to rectify this situation.

## 6. Concluding Remarks

We use satellite magnetic field data from the recent Lunar Prospector and Kaguya Selene missions to demonstrate that the magnetic field in the geomagnetic tail is well organized, and can be described with a degree and order one spherical harmonic geometry. Assuming further that the magnetic field in the geomagnetic tail is predominantly potential, we were able to estimate global  $C$ -responses from the satellite data, using a conventional geomagnetic depth sounding technique. This is in contrast to the approach during the Apollo era, which required simultaneous magnetic field measurements at the surface and from an orbiter. Inversion of the estimated  $C$ -responses allowed us to infer the first global radial electrical conductivity profile of the lunar upper and mid-mantle; the conductivity is constrained in the depth range of ~300–900 km.

**Table 4**

Depth, Electrical Conductivity, and 95% Confidence Intervals of the Conductivity Values for the Smooth and the Sparse Models

Depth (km)	Smooth model			Sparse model		
	$\sigma$ (S/m)	$\sigma_{lower}$ (S/m)	$\sigma_{upper}$ (S/m)	$\sigma$ (S/m)	$\sigma_{lower}$ (S/m)	$\sigma_{upper}$ (S/m)
0	0.000512	0.000335	0.000783	0.000388	0.000249	0.000602
40	0.000512	0.000339	0.000772	0.000388	0.000253	0.000594
80	0.000512	0.000348	0.000754	0.000391	0.000262	0.000585
120	0.000512	0.000354	0.000740	0.000399	0.000273	0.000583
160	0.000513	0.000360	0.000731	0.000412	0.000287	0.000591
200	0.000515	0.000365	0.000726	0.000431	0.000305	0.000610
240	0.000517	0.000369	0.000724	0.000459	0.000328	0.000640
280	0.000522	0.000374	0.000728	0.000496	0.000358	0.000686
320	0.000527	0.000379	0.000733	0.000545	0.000397	0.000748
360	0.000532	0.000383	0.000739	0.000610	0.000447	0.000833
400	0.000589	0.000424	0.000818	0.000695	0.000511	0.000946
440	0.000680	0.000490	0.000943	0.000809	0.000596	0.00110
480	0.000851	0.000614	0.00118	0.000960	0.000709	0.00130
520	0.00112	0.000809	0.00154	0.00116	0.000861	0.00157
560	0.00148	0.00108	0.00204	0.00144	0.00107	0.00194
600	0.00181	0.00133	0.00248	0.00183	0.00136	0.00246
640	0.00234	0.00172	0.00319	0.00239	0.00178	0.00320
680	0.00265	0.00196	0.00357	0.00321	0.00241	0.00429
720	0.00304	0.00227	0.00407	0.00445	0.00335	0.00590
760	0.00371	0.00280	0.00490	0.00637	0.00485	0.00839
800	0.00488	0.00374	0.00637	0.00943	0.00724	0.0123
840	0.00804	0.00625	0.0104	0.0143	0.0111	0.0185
880	0.0150	0.0118	0.0190	0.0220	0.0173	0.0279
920	0.0320	0.0257	0.0400	0.0333	0.0265	0.0418
960	0.0639	0.0519	0.0787	0.0484	0.0389	0.0601
1,000	0.0929	0.0760	0.114	0.0649	0.0525	0.0802
1,040	0.0930	0.0756	0.114	0.0788	0.0636	0.0977
1,080	0.0931	0.0743	0.117	0.0878	0.0699	0.110
1,120	0.0931	0.0723	0.120	0.0921	0.0719	0.118
1,160	0.0931	0.0701	0.124	0.0938	0.0713	0.123
1,200	0.0931	0.0679	0.128	0.0943	0.0695	0.128

While our new transfer function is limited in period range relative to what was derived from Apollo data, but extended through the estimation of both real and imaginary parts of the responses, the apparent resistivities deduced from our and the Apollo-based transfer functions are found to agree remarkably well. This serves to emphasize consistency between the earlier and the novel transfer functions presented here.

Planned missions to equip the Moon with several geophysical surface stations are underway (Weber et al., 2020). Such mission opportunities are vital to further explore the interior structure by providing several long-lived platforms distributed across the Moon and to enable a range of geophysical experiments. It is important to stress that the approach described in this study is easily adaptable to estimate local  $C$ -responses using surface magnetic field data only. Future lunar electromagnetic induction studies will also significantly benefit from higher-frequency magnetic field measurements, including the potential addition

of electric field measurements (Grimm & Delory, 2012). In particular, this will enable derivation of ground transfer functions at shorter periods to constrain electrical structure of the crust and uppermost mantle to a depth of  $\sim 300$  km. New constraints on the near-surface structure are particularly important in the context of resource evaluation and a lunar base. Furthermore, several long-lived ground stations will ensure multiple local studies that together will provide context for a global understanding of the lunar interior.

## Data Availability Statement

All LP and KS data used in this study are publicly available, and we appreciate the effort of the spacecraft teams in collecting and archiving the data. LP data are archived in the Planetary Data System (<https://doi.org/10.17189/1519723>; Hood, 2003), and KS data are archived by the Japanese Aerospace Exploration Agency (<https://data.darts.isas.jaxa.jp/pub/pds3/sln-l-lmag-3-mag-ts-v1.0/>).

## Acknowledgments

A. Mittelholz acknowledges support from ETH 19-2 FEL-34. A. Grayver acknowledges support from ETH ETH-12 18-1. A. Grayver and A. Kuvshinov were also supported in the framework of Swarm DISC activities, funded by ESA contract number 4000109587, with support from EO Science for Society program. The authors thank L. Hood and T. Ravat for helpful comments. Open access funding provided by Eidgenössische Technische Hochschule Zurich.

## References

- Banks, R. J. (1969). Geomagnetic variations and the electrical conductivity of the upper mantle. *Geophysical Journal International*, 17(5), 457–487. <https://doi.org/10.1111/j.1365-246X.1969.tb00252.x>
- Baumjohann, W., & Treumann, R. A. (1996). *Basic space plasma physics*. Imperial College Press and Distributed by World Scientific Publishing Co. <https://www.worldscientific.com/doi/abs/10.1142/p015>
- Connolly, J. A. D. (2005). Computation of phase equilibria by linear programming: A tool for geodynamic modeling and its application to subduction zone decarbonation. *Earth and Planetary Science Letters*, 236(1), 524–541. <https://doi.org/10.1016/j.epsl.2005.04.033>
- Daily, W. D., & Dyal, P. (1979). Magnetometer data errors and lunar induction studies. *Journal of Geophysical Research*, 84(A7), 3313–3326. <https://doi.org/10.1029/JA084ia07p03313>
- Dyal, P., Parkin, C., & Daily, W. (1976). Structure of the lunar interior from magnetic field measurements. *Lunar and Planetary Science Conference Proceedings*, 3, 3077–3095.
- Dyal, P., Parkin, C. W., & Daily, W. D. (1974). Magnetism and the interior of the Moon. *Reviews of Geophysics*, 12(4), 568–591. <https://doi.org/10.1029/RG012i004p00568>
- Grayver, A. V., & Kuvshinov, A. V. (2016). Exploring equivalence domain in nonlinear inverse problems using Covariance Matrix Adaption Evolution Strategy (CMAES) and random sampling. *Geophysical Journal International*, 205(2), 971–987. <https://doi.org/10.1093/gji/ggw063>
- Grimm, R. E., & Delory, G. T. (2012). Next-generation electromagnetic sounding of the Moon. *Advances in Space Research*, 50(12), 1687–1701. <https://doi.org/10.1016/j.asr.2011.12.014>
- Guzavina, M., Grayver, A., & Kuvshinov, A. (2019). Probing upper mantle electrical conductivity with daily magnetic variations using global-to-local transfer functions. *Geophysical Journal International*, 219(3), 2125–2147. <https://doi.org/10.1093/gji/ggz412>
- Hobbs, B. A. (1973). The inverse problem of the Moon's electrical conductivity. *Earth and Planetary Science Letters*, 17(2), 380–384. [https://doi.org/10.1016/0012-821x\(73\)90204-5](https://doi.org/10.1016/0012-821x(73)90204-5)
- Hobbs, B. A. (1977). The electrical conductivity of the Moon: An application of inverse theory. *Geophysical Journal International*, 51(3), 727–744. <https://doi.org/10.1111/j.1365-246X.1977.tb04217.x>
- Hobbs, B. A., Hood, L. L., Herbert, F., & Sonett, C. P. (1983). An upper bound on the radius of a highly electrically conducting lunar core. *Journal of Geophysical Research*, 88(B97), 97–102. <https://doi.org/10.1029/JB088is01p00b97>
- Holland, T. J. B., & Powell, R. (1998). An internally consistent thermodynamic data set for phases of petrological interest. *Journal of Metamorphic Geology*, 16(3), 309–343.
- Hood, L. (2003). *LP moon MAG level 4 lunar magnetic field time series V1.0*. NASA Planetary Data System. <https://doi.org/10.17189/1519723>
- Hood, L., Herbert, F., & Sonett, C. P. (1982a). The deep lunar electrical conductivity profile: Structural and thermal inferences. *Journal of Geophysical Research*, 87(B7), 5311–5326. <https://doi.org/10.1029/JB087ib07p05311>
- Hood, L., Herbert, F., & Sonett, C. P. (1982b). Further efforts to limit lunar internal temperatures from electrical conductivity determinations. *Journal of Geophysical Research*, 87, A109–A116. <https://doi.org/10.1029/JB087is01p0a109>
- Hood, L., Zakharian, A., Halekas, J., Mitchell, D. L., Lin, R. P., Acuña, M. H., & Binder, A. B. (2001). Initial mapping and interpretation of lunar crustal magnetic anomalies using Lunar Prospector magnetometer data. *Journal of Geophysical Research*, 106(E11), 27825–27839. <https://doi.org/10.1029/2000JE001366>
- Hood, L., & Zuber, M. T. (2000). Recent refinements in geophysical constraints on lunar origin and evolution. *Origin of the Earth and Moon*, 397–410. <https://doi.org/10.2307/j.ctv1vzdpr.26>
- Hood, L. L., Mitchell, D. L., Lin, R. P., Acuna, M. H., & Binder, A. B. (1999). Initial measurements of the lunar induced magnetic dipole moment using Lunar Prospector magnetometer data. *Geophysical Research Letters*, 26(15), 2327–2330. <https://doi.org/10.1029/1999GL900487>
- Hood, L. L., & Schubert, G. (1978). A magnetohydrodynamic theory for the lunar response to time variations in a spatially uniform ambient magnetic field. In *Lunar and Planetary Science Conference Proceedings* (Vol. 9, pp. 3125–3135).
- Jaumann, R., Hiesinger, H., Anand, M., Crawford, I. A., Wagner, R., Sohl, F., et al. (2012). Geology, geochemistry, and geophysics of the Moon: Status of current understanding. *Planetary and Space Science*, 74(1), 15–41. <https://doi.org/10.1016/j.pss.2012.08.019>
- Jutzi, M., & Asphaug, E. (2011). Forming the lunar farside highlands by accretion of a companion moon. *Nature*, 476(7358), 69–72. <https://doi.org/10.1038/nature10289>
- Khan, A., Connolly, J. A. D., Olsen, N., & Mosegaard, K. (2006). Constraining the composition and thermal state of the Moon from an inversion of electromagnetic lunar day-side transfer functions. *Earth and Planetary Science Letters*, 248, 579–598. <https://doi.org/10.1016/j.epsl.2006.04.008>
- Khan, A., Connolly, J. A. D., Pommier, A., & Noir, J. (2014). Geophysical evidence for melt in the deep lunar interior and implications for lunar evolution. *Journal of Geophysical Research: Planets*, 119, 2197–2221. <https://doi.org/10.1002/2014JE004661>
- Khan, A., Pommier, A., Neumann, G. A., & Mosegaard, K. (2013). The lunar Moho and the internal structure of the Moon: A geophysical perspective. *Tectonophysics*, 609, 331–352. <https://doi.org/10.1016/j.tecto.2013.02.024>

- Kuvshinov, A., Grayver, A., Tøffner-Clausen, L., & Olsen, N. (2021). Probing 3-D electrical conductivity of the mantle using 6 years of Swarm, CryoSat-2 and observatory magnetic data and exploiting matrix Q-responses approach. *Earth Planets and Space*, 73(1), 67. <https://doi.org/10.1186/s40623-020-01341-9>
- Kuvshinov, A., & Semenov, A. (2012). Global 3-D imaging of mantle electrical conductivity based on inversion of observatory C-responses—I. An approach and its verification. *Geophysical Journal International*, 189(3), 1335–1352. <https://doi.org/10.1111/j.1365-246X.2011.05349.x>
- Longhi, J. (2003). A new view of lunar ferroan anorthosites: Postmagma ocean petrogenesis. *Journal of Geophysical Research*, 108(E8), 5083. <https://doi.org/10.1029/2002JE001941>
- Mosegaard, K., & Tarantola, A. (1995). Monte Carlo sampling of solutions to inverse problems. *Journal of Geophysical Research*, 100(B7), 12431–12447. <https://doi.org/10.1029/94JB03097>
- Munch, F. D., Grayver, A. V., Kuvshinov, A., & Khan, A. (2018). Stochastic inversion of geomagnetic observatory data including rigorous treatment of the ocean induction effect with implications for transition zone water content and thermal structure. *Journal of Geophysical Research: Solid Earth*, 123, 31–51. <https://doi.org/10.1002/2017JB014691>
- Nagihara, S., Williams, D. R., Nakamura, Y., Kiefer, W. S., McLaughlin, S. A., & Taylor, P. T. (2020). Availability of previously lost data and metadata from the Apollo Lunar Surface Experiments Package (ALSEP). *Planetary and Space Science*, 191, 105039. <https://doi.org/10.1016/j.pss.2020.105039>
- Nakamura, R., Yamamoto, S., Matsunaga, T., Ishihara, Y., Morota, T., Hiroi, T., et al. (2012). Compositional evidence for an impact origin of the Moon's Procellarum basin. *Nature Geoscience*, 5(11), 775–778. <https://doi.org/10.1038/ngeo1614>
- NASA. (2008). *A standardized lunar coordinate system for the lunar reconnaissance orbiter and lunar datasets. LRO project and LGCWG white paper (Tech. Rep.)*. Retrieved from <http://lunar.gsfc.nasa.gov/library/LunCoordWhitePaper-10-08.pdf>
- Ness, N. F., Behannon, K. W., Cantarano, S. C., & Scearce, C. S. (1967). Observations of the Earth's magnetic tail and neutral sheet at 510,000 kilometers by Explorer 33. *Journal of Geophysical Research*, 72(3), 927–933. <https://doi.org/10.1029/JZ072i003p00927>
- Olsen, N. (1999). Induction studies with satellite data. *Surveys in Geophysics*, 20(3–4), 309–340. <https://doi.org/10.1023/A:1006611303582>
- Price, A. T. (1967). II-3—Electromagnetic induction within the Earth. In S. Matsushita, & W. H. Campbell (Eds.), *Physics of geomagnetic phenomena* (Vol. 11, pp. 235–298). Academic Press. <https://doi.org/10.1016/b978-0-12-480301-5.50012-4>
- Pütte, C., & Kuvshinov, A. (2014). Mapping 3-D mantle electrical conductivity from space: A new 3-D inversion scheme based on analysis of matrix Q-responses. *Geophysical Journal International*, 197(2), 768–784. <https://doi.org/10.1093/gji/ggu027>
- Ravat, D., Purucker, M. E., & Olsen, N. (2020). Lunar magnetic field models from Lunar Prospector and Selene/Kaguya along-track magnetic field gradients. *Journal of Geophysical Research: Planets*, 125, e2019JE006187. <https://doi.org/10.1029/2019JE006187>
- Russell, C. T., Coleman, P. J., & Goldstein, B. E. (1981). Measurements of the lunar induced magnetic moment in the geomagnetic tail: Evidence for a lunar core? *Lunar and Planetary Science Conference Proceedings*, 12, 831–836.
- Shimizu, H., Matsushima, M., Takahashi, F., Shibuya, H., & Tsunakawa, H. (2013). Constraint on the lunar core size from electromagnetic sounding based on magnetic field observations by an orbiting satellite. *Icarus*, 222(1), 32–43. <https://doi.org/10.1016/j.icarus.2012.10.029>
- Sonett, C. P. (1982). Electromagnetic induction in the Moon. *Reviews of Geophysics*, 20(3), 411–455. <https://doi.org/10.1029/RG020i003p00411>
- Sonett, C. P., Colburn, D. S., Dyal, P., Parkin, C. W., Smith, B. F., Schubert, G., & Schwartz, K. (1971). Lunar electrical conductivity profile. *Nature*, 230(5293), 359–362. <https://doi.org/10.1038/230359a0>
- Sonett, C. P., Smith, B. F., Colburn, D. S., Schubert, G., & Schwartz, K. (1972). The induced magnetic field of the moon: Conductivity profiles and inferred temperature. In *Lunar and Planetary Science Conference Proceedings* (Vol. 3, p. 2309).
- Takahashi, F., Shimizu, H., Matsushima, M., Shibuya, H., Matsuoka, A., Nakazawa, S., et al. (2009). In-orbit calibration of the lunar magnetometer onboard Selene (Kaguya). *Earth Planets and Space*, 61(11), 1269–1274. <https://doi.org/10.1186/BF03352979>
- Tapping, K. F. (2013). The 10.7 cm solar radio flux (F10.7). *Space Weather*, 11, 394–406. <https://doi.org/10.1002/swe.20064>
- Taylor, S. R. (1982). *Planetary science: A lunar perspective*. Citeseer.
- Verhoeven, O., Rivoldini, A., Vacher, P., Mocquet, A., Choblet, G., Menyelle, M., & Lognonné, P. (2005). Interior structure of terrestrial planets: Modeling Mars' mantle and its electromagnetic, geodetic, and seismic properties. *Journal of Geophysical Research*, 110, E04009. <https://doi.org/10.1029/2004JE002271>
- Weber, R. C., Lin, P. Y., Garnero, E. J., Williams, Q., & Lognonné, P. (2011). Seismic detection of the lunar core. *Science*, 331(6015), 309–312. <https://doi.org/10.1126/science.1199375>
- Weber, R. C., Neal, C., Banerdt, B., Beghein, C., Chi, P., Currie, D., & Grimm, R. (2020). The lunar geophysical network mission. In *Seg technical program expanded abstracts 2020* (pp. 3530–3533). Society of Exploration Geophysicists. <https://doi.org/10.1190/segam2020-3416702.1>
- Weidelt, P. (1972). The inverse problem of geomagnetic induction. *Journal of Geophysics*, 38, 257–289.
- Whitaker, E. A. (1981). The lunar Procellarum basin. In *Multi-ring basins: Formation and evolution* (pp. 105–111).
- Xu, Y., Shankland, T. J., & Poe, B. T. (2000). Laboratory-based electrical conductivity in the Earth's mantle. *Journal of Geophysical Research*, 105(B12), 27865–27875. <https://doi.org/10.1029/2000JB900299>